Materials Characterization 140 (2018) 233–246

Contents lists available at ScienceDirect

Materials Characterization

journal homepage: www.elsevier.com/locate/matchar

On the microstructure characterization of the AA2098-T351 alloy welded by FSW

Mariana X. Milagre[a,*], Naga V. Mogili[b], Uyime Donatus[a], Rafael A.R. Giorjão[b], Maysa Terada[b], João Victor S. Araujo[a], Caruline S.C. Machado[a], Isolda Costa[a]

[a] Instituto de Pesquisas Energéticas e Nucleares – IPEN/CNEN, Av. Prof. Lineu Prestes, 2242 São Paulo, Brazil
[b] Laboratório Nacional de Nanotecnologia – LNNANO/CNPEM, R. Giuseppe Máximo Scolfaro, 10.000 Campinas, Brazil

ARTICLE INFO

Keywords:
A. characterization
A. thermal analysis
A. hardness
B. aluminum alloys

ABSTRACT

The complex structure of the AA2098-T351 alloy welded by friction stir welding (FSW) was investigated by transmission electron microscopy (TEM), differential scanning calorimetry (DSC) and microhardness measurements. Thermal modelling process of the FSW process was carried out by soldering thermocouples at distances of 6, 9 and 12 mm from the weld centerline, and thermocouple measurements were used as input data into the model. Finite element software COMSOL v5.2 was used for data analysis. The prevailing phases in the base metal (BM) are T1 (Al_2CuLi) θ′ (Al_2Cu), δ′/β′(Al_3(Li,Zr)) and Ω (Al_2Cu). In the heat affected zone (HAZ), either in the retreating or advancing sides, θ′ phase was not identified. In the thermomechanical affected zone (TMAZ), T1, δ′/β′, GP zones phase were detected in the retreating side, whereas T1 and Guinier-Preston (GP) zones were not observed in the advancing side. This result supports the asymmetric behavior observed in the microhardness profile of the weld. In the stir zone (SZ), GP zones, T1, δ′/β′ (Al_3(Li,Zr)) and Ω were identified.

1. Introduction

Friction stir welding (FSW) was developed as an alternative to conventional welding processes and it was found to be more advantageous for welding Al alloys. FSW generates aluminum welding joints with superior mechanical properties [1–3]. This process is characterized by the insertion of a non-consumable rotating tool, comprising a pin and a shoulder, which traverses the abutting joint of the materials to be welded. The intense plastic deformation and high temperatures reached modifies the microstructural features of the welded surface; consequently, different welding zones, such as the stir zone (SZ), thermomechanical affected zone (TMAZ), heat affected zone (HAZ), in addition to the unaffected material, known as the base metal (BM) are produced [1–5].

The SZ is characterized by intense heating and plastic deformation that lead to dynamic recrystallization with fine grains and phase dissolution (in most cases, especially if the alloy is a precipitation hardened alloy). In the TMAZ, the degree of deformation and temperature attained lead to heavily deformed grains and phase dissolution depending on the alloy system. Unlike the SZ, recrystallization does not occur in the TMAZ. In the HAZ, the lack of plastic deformation results in grains with similar shape compared with that of the BM. Nonetheless, the HAZ experiences temperatures high enough to cause precipitate dissolution, coarsening and the formation of precipitate free zone (PFZ) is sometimes observed. In the BM, thermal cycles may be experienced but they are not sufficient enough to cause changes in microstructure or mechanical properties [2–4].

Modifications in microstructural features due to welding processes have been reported by many authors [6–9]. However, these changes are influenced by the welding parameters adopted [6]; consequently, each welding process is unique. For instance, Cavalieri et al. [7] analyzed the phases present in AA2198 welded by FSW using selected area electron diffraction (SAED). They found θ′ (Al_2Cu) and δ′ (Al_3Li) in the SZ, and θ′ (Al_2Cu), δ′ (Al_3Li) and T1 (Al_2CuLi) in the TMAZ and HAZ. Further, Gao et al. (2015) also reported the presence of β′(Al_3Zr) in the HAZ and δ′ and β′ in the SZ of AA2198. Li et al. [8] detected T1 phase in the SZ of AA2198 [8]. Rao et al. [9] also reported the presence of T1 and T_B phases in the SZ of AA2198. Based on literature [6–8], it can be concluded that there is no general agreement on the microstructural features of each welded zone due to the influence of welding parameters. As mentioned earlier, every case is unique, and for the new generation Al-Cu-Li alloys, establishing the microstructural features responsible for their in-service performances is far from being complete. Further, the precipitation sequence of this group of alloys is complex since they possess more than one strengthening precipitates which are precipitated and dissolved at varying temperatures and states of stress

* Corresponding author.
E-mail address: marianamilagre@yahoo.com.br (M.X. Milagre).

https://doi.org/10.1016/j.matchar.2018.04.015
Received 25 February 2018; Received in revised form 31 March 2018; Accepted 10 April 2018
Available online 11 April 2018

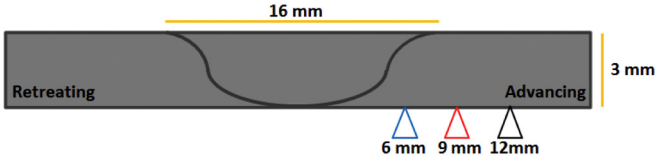

Fig. 1. Schematic diagram of thermocouples positioning in the welded AA2098-T351 alloy.

[10,11]. Consequently, it is of major importance to further characterize the complex microstructure of new generation Al-Cu-Li alloys (which is even more complex when welded by FSW). This is important as these alloys are aerospace alloys and the overall performance of their welds is heavily dependent on produced microstructural features which are yet to be fully established.

Considering the importance of nano-sized phases on the corrosion and mechanical properties of aluminum-copper-lithium alloys, the transmission electron microscopy (TEM) is crucial in microstructural characterization of these alloys. TEM has been largely used in the investigation of phases in each of the welded zones [4,7–9,12–14]. Differential scanning calorimetry (DSC) has also been applied to microstructural characterization of light metals, such as Al alloys [15–28]. According to Starink [17], DSC is useful in the study of solid state reactions that occur during processing of Al alloys (solidification, homogenization, precipitation). Moreover, this technique is effective in the study of heat treatments of Al alloys since it provides useful information on the temperature ranges for phase dissolution and precipitation. Sidhar et al. [28] used DSC to characterize the precipitates in differently heat-treated Al-Cu-Li-Mg-Ag and Al-Cu-Li-Mg alloys that were welded by FSW. This technique was also used by Qui et al. [20] for microstructural characterization of the weld affected zones of 2195-T8 Al–Li alloy.

There are many published works on the microstructure of the AA2198 alloy [7–9,12,29–33]. This alloy is derived from the AA2098 used in this study. However, it contains slightly lower copper contents compared to the AA2098 alloy [31,32]. It must be mentioned that the literature on microstructural features of the AA2098 alloy is scarce [34,35]. Therefore, the aim of the present study is to provide this lack of information on the microstructure of the AA2098-T351 alloy welded by FSW. This investigation was carried out using TEM and DSC analyses, in

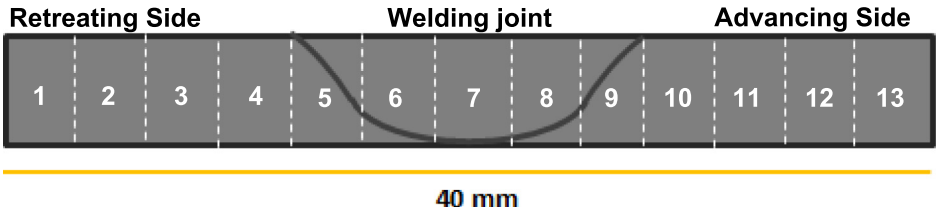

Fig. 2. Schematic diagram of the different positions from which FSW AA2098-T351 alloy samples were obtained for DSC analysis.

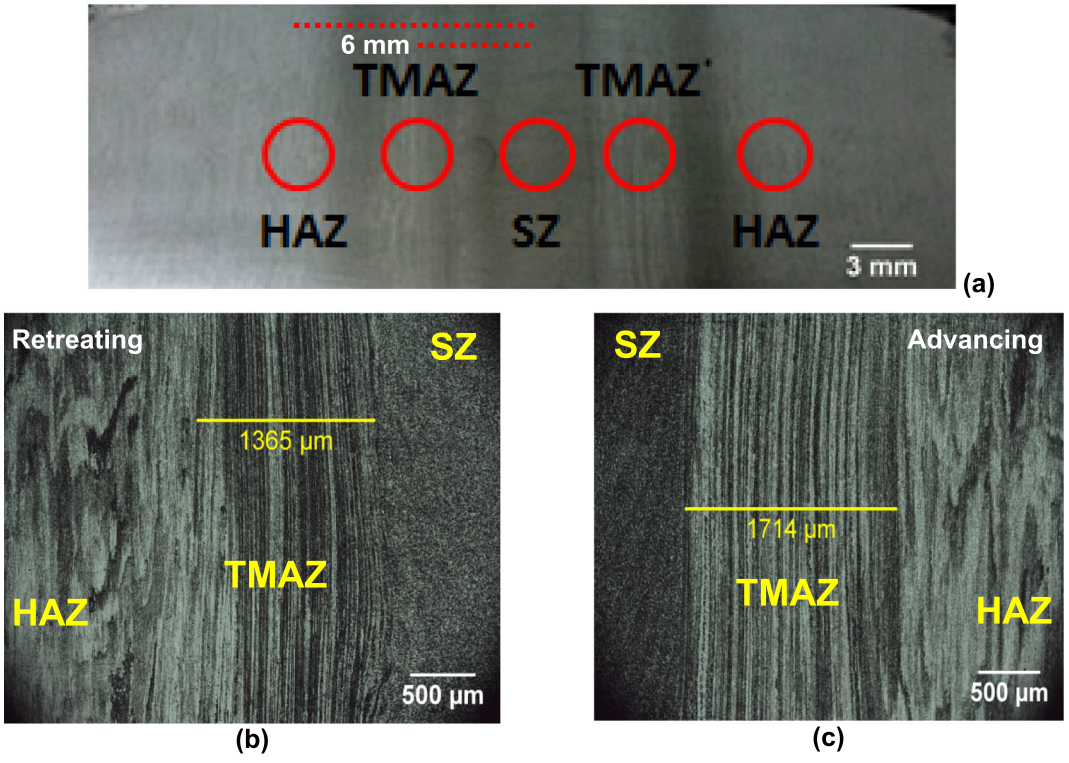

Fig. 3. (a) Macroscopic image of the welded sample indicating the areas from which samples for TEM analysis were obtained. (b) TMAZ width from retreating side; (c) TMAZ width from advancing side.

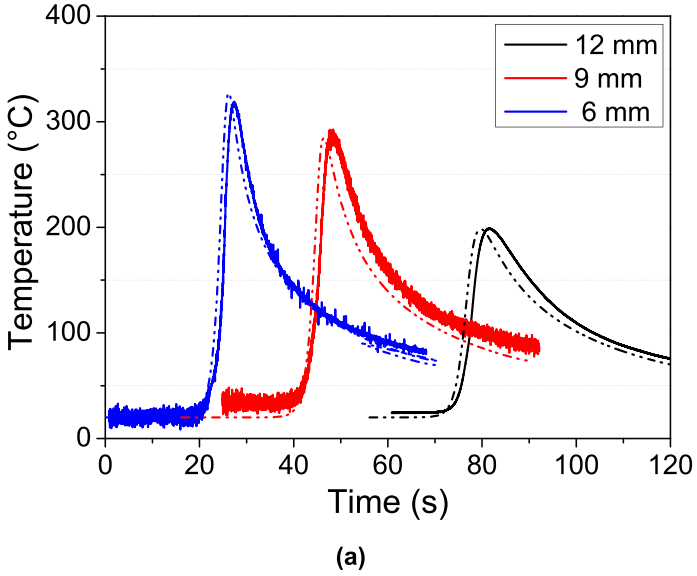

(a)

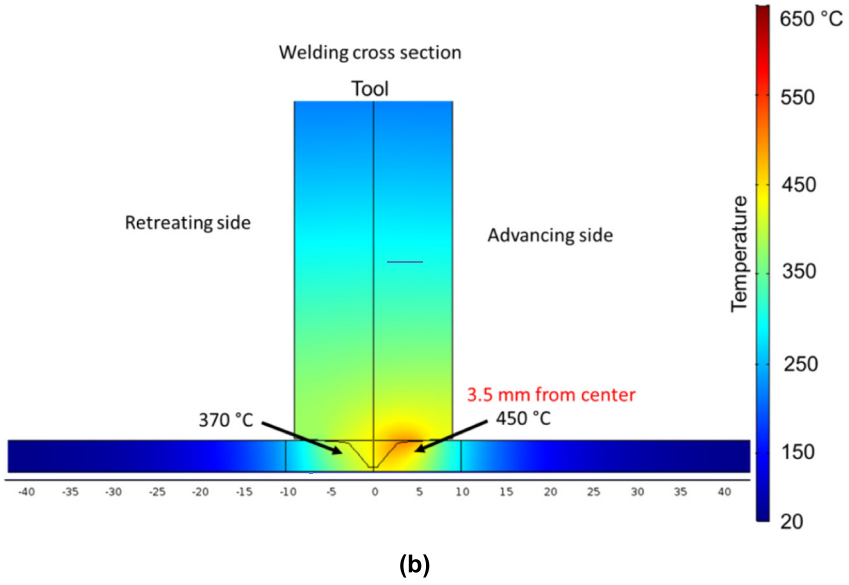

(b)

Fig. 4. Results obtained from thermal profile simulation: (a) temperature variation with time at different distances from the joint from thermal modelling (dashed lines) and from measurements using thermocouples (solid line); (b) thermal modelling results from cross-sectional view of the trailing edge.

addition to microhardness measurements and thermal simulation of the FSW process adopted in this study, to correlate the microstructure to the FSW effects.

2. Materials and Methods

2.1. Material

The AA2098-T351 alloy (3.4 wt% Cu, 1 wt% Li, 0.3 wt% Mg, 0.3% wt Ag, 0.4 wt% Zr, 0.04 wt% Fe, 0.05 wt% Si, 0.02 wt% Zn, 0.003 wt% Mn) was used in this work. The temper T351 corresponds to (1) Solution heat treatment; (2) stress relief by stretching; and (3) natural aging.

2.2. Friction Stir Welding (FSW)

The friction stir welding process was modeled using as a steady-state visco-plastic laminar flow in a computational fluid dynamics (CFD) package. The CFD method allows to simulate the material flow pattern in FSW coupled with thermal simulation. This method has already reported good results simulating both temperature and material flow pattern by Nandan et al., [36] and others [37–40]. The fundamental assumption in is that the flow of the sheet material resembles that of a non-Newtonian and highly viscous fluid.

The model in the present work provides temperatures distribution by a fully coupled thermal–mechanical model based on CFD using COMSOL v5.2 software [36]. Simulated temperature results were compared with reference experimental data obtained by thermocouples positioned as shown in Fig. 1. In order to validate the model, the same process parameters for simulations and experiments were chosen to

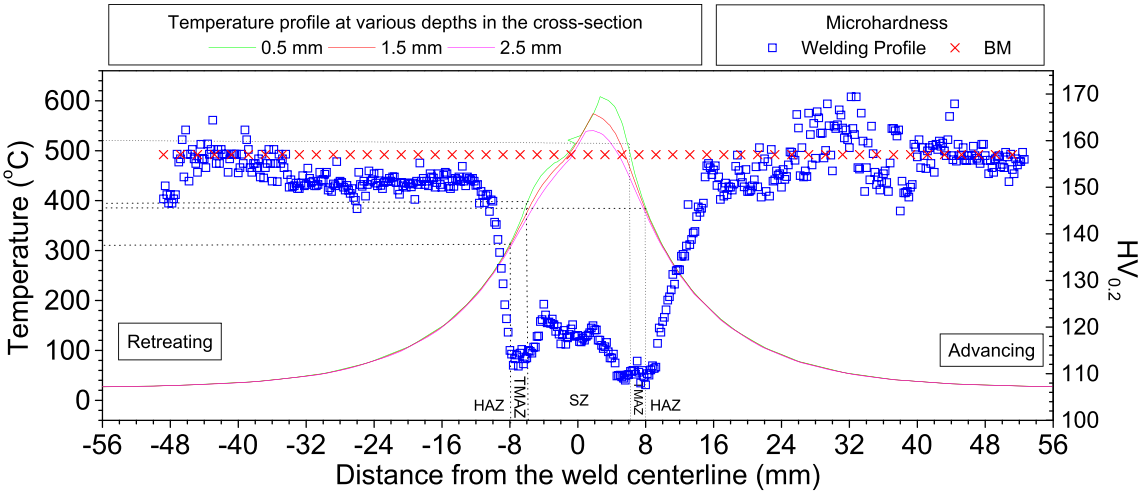

Fig. 5. Relationship between top surface microhardness profile and temperatures calculated at different depths from the cross-section of FSWelded AA2098-T351 alloy.

Table 1
Extrapolation of temperature reached in each welding zone.

Welding zone	Temperatures reached (°C)
HAZ (RS)	< 300
TMAZ (RS)	400–300
SZ	600–400
TMAZ (AS)	520–380
HAZ (AS)	< 380

compare temperatures.

Physical phenomena in welding, such as heat transfer by conduction and radiation, were considered. The welding model counted 86,009 elements. The thermal conductivity and specific heat of the AA2024 alloy were used as references in the COMSOL database, once the data for the AA2098 alloy used in this work are not available.

The temperature and velocity field were solved assuming steady-state behavior. Viscosity is determined using the flow stress (σ_e) and the effective strain rate $\dot{\varepsilon}$ as follows:

$$\mu = \frac{\sigma_e}{3\dot{\varepsilon}} \tag{1}$$

The flow stress in a perfectly plastic model was proposed by Sellars [41]:

$$\sigma_e = \frac{1}{\alpha} sin\, h^{-1}\left[\left(\frac{Z}{A}\right)^{1/n}\right] \tag{2}$$

Z is the Zener–Hollomon parameter which is an empirical function of temperature and strain rates as shown below

$$Z = \dot{\varepsilon}\exp\left(\frac{Q}{RT}\right) \tag{3}$$

where Q is the activation energy of lattice diffusion and R is the universal gas constant. The values of Q and A were taken from Yang et al. [42]. In the simulation model, the heat is generated due to plastic dissipation which increases as the strain rate increases. In addition, the full sticking conditions assumed in this work will result in extremely high strain rates and temperatures [43].

2.3. Microhardness Test

Microhardness measurements were recorded from the sample surface in steps of 0.2 mm using a load of 200 gf for a dwell time of 10 s. A Knoop/Vickers Tukon 1202 Wilson Hardness was employed for this purpose. Three sets of measurements were recorded at the surface, and their mean values were estimated.

2.4. Differential Scanning Calorimetry (DSC)

DSC data were obtained in nitrogen (99.999 wt%) atmosphere using a 822 Mettler Toledo equipment. Samples were ground with silicon carbide paper. The weights of the samples employed for the test were in the range of 20–30 mg. The heating rate used in the DSC measurements was 10 °C/min and the scanning temperature range was from 50 °C to 550 °C. Samples used for DSC measurements were removed from different regions along the welded sample, as indicated in Fig. 2 by numbers. Samples from the unwelded alloy were also tested by DSC for comparison.

2.5. Transmission Electron Microscopy (TEM)

Discs of 3 mm diameters were used for TEM analysis as shown in Fig. 3a. Fig. 3b–c are magnified images of the selected TMAZ regions of the advancing side (AS) and retreating side (RS) in Fig. 3a, respectively. Electrolytic etching was performed in a solution composed of 20% nitric acid in methanol at 25 V and at −30 °C prior to acquisition of transmission electron microscopy (TEM) images. TEM samples were prepared using a TenuPol equipment. The imaging was carried out using a JEOL 2100 microscope. Selected area electron diffraction (SAED) patterns were recorded with a Gatan ES500W camera. Images were acquired using a TVIPS F416 4 K × 4 K camera, and for specimen tilting, a JEOL EM 31630 double tilt holder was used. All the weak reflections related to the superlattice spots in SAED patterns were enhanced using DiffTools plugin [44] in digital micrograph software.

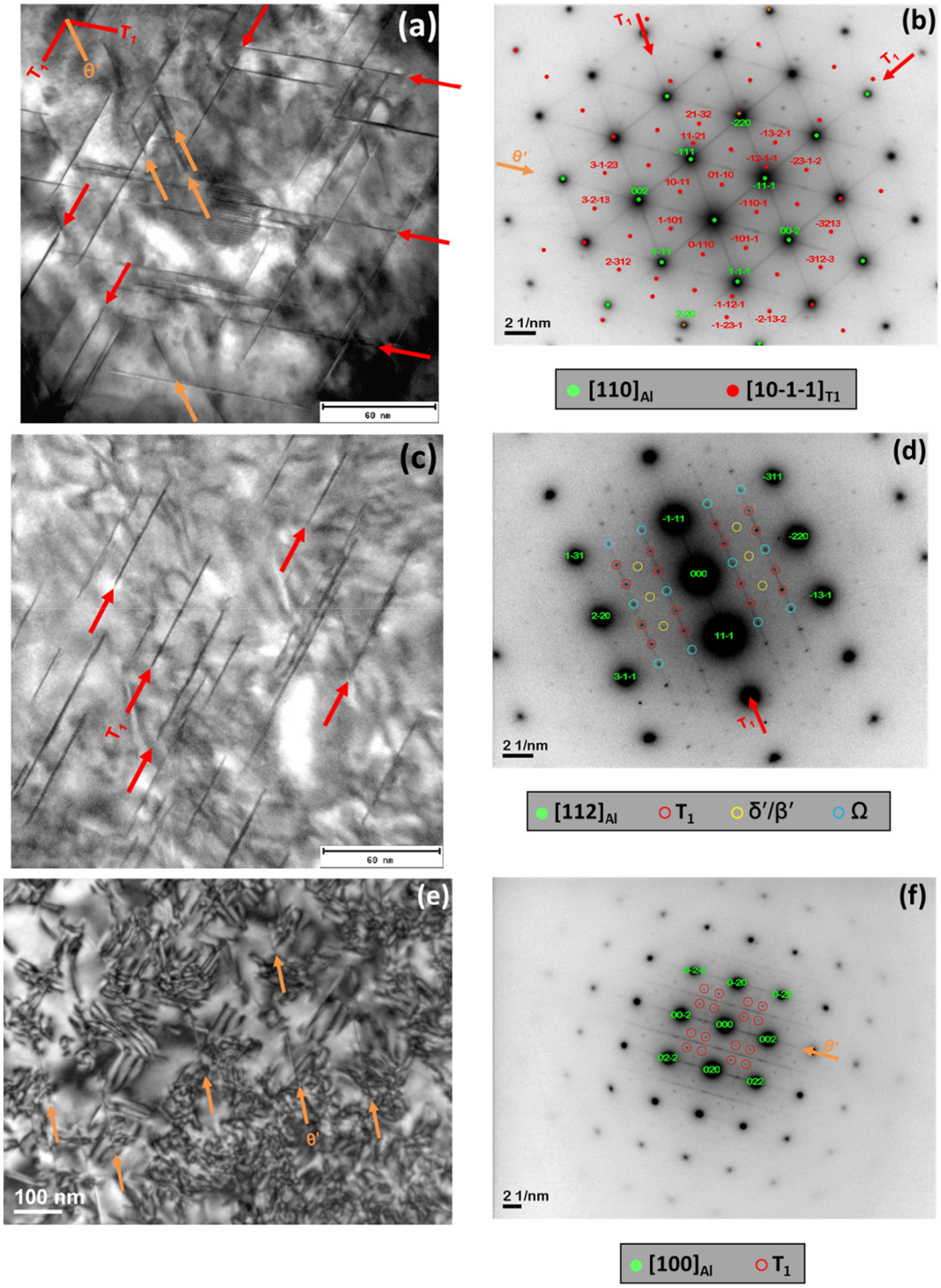

Fig. 6. TEM bright field images (a, c, e) and SAED patterns (b, d, f) obtained in [110], [112], [100] orientations showing the dominant phases in unwelded (BM) AA2098-T351 alloy. T1 and θ′ variants appear differently in various orientations; when viewed along [110] orientation (a, b), two T1 variants and one θ′ variant appear edge-on; in [112] zone axis (c, d), one T1 variant (out of 4) was observed edge-on, whereas in [100] zone axis (e, f), one θ′ variant was observed edge-on.

3. Results and Discussion

3.1. Thermal Simulation

Results of thermal modelling are shown in Fig. 4. Temperatures indicated by thermal simulation are consistent with those obtained by measurements using thermocouples in their corresponding positions, Fig. 4a. Thermal cycle acquisition and thermal distribution are much important for investigation of metallurgical transformations and determination of extension of these transformations. The measured temperatures validated the thermal simulation. It can be noted that temperature effects are found even at large distances from the weld joint. Moreover, the advancing side reaches higher temperatures than the retreating side, Fig. 4b, as already described by other authors [7,13,45].

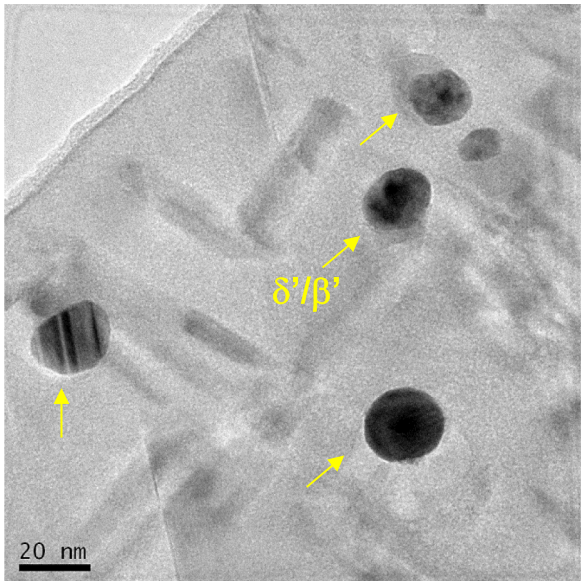

Fig. 7. TEM bright field image showing δ′/β′ core-shell morphology.

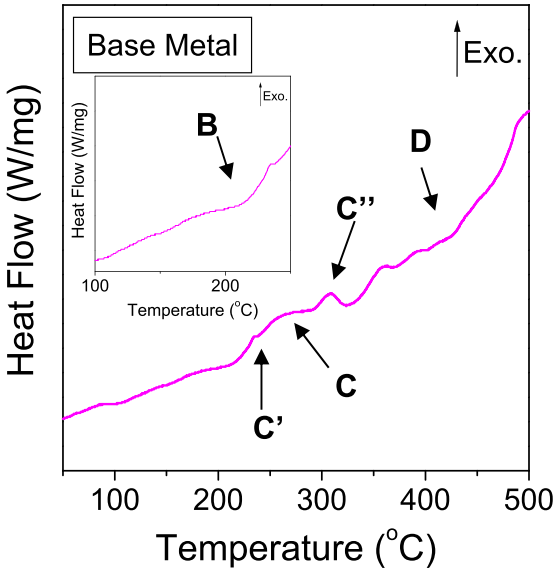

Fig. 8. DSC thermograms obtained at 10 °C/min from the AA2098-T351 alloy (BM). The dimensions of each sample were 3 mm × 3 mm × 1 mm.

The temperatures indicated in Fig. 4b are representative of the trailing edge distribution. During the welding process, the tool moves by rotation and translation. At the AS the rotating tool experiences more resistance to the translational movement of the tool and somewhat dwells longer at the AS [46]. This leads to more heat generation at the AS compared with the RS.

3.2. Microhardness

The relationship between welding process temperatures and microstructural variations is evident in Fig. 5. At the welding joint, the high temperatures reached are responsible for the decreased microhardness. This behavior has been described by many authors [4,7,8,47]. The microhardness at 16 mm from the weld centerline (0 mm) dropped compared with that of the BM. Given that the T1 phase is the predominant strengthening phase in Al-Cu-Li alloys [5,13,14], this behavior is typical of overaging that leads to T1 phase coarsening and partial dissolution in addition to other phase dissolution [4,7,20]. In the retreating side of the TMAZ, temperatures reached values between 400 °C and 300 °C, Table 1, and at this temperature range the majority of T1 phase seems to be dissolved and others could have been partially coarsened, as proposed by Chen et al. [27]. In the advancing side of the TMAZ, the temperatures reached values in the range from 520 °C to 380 °C, Table 1, that is, temperatures higher than that of T1 dissolution [12,27], leading to low microhardness values. This asymmetric behavior between advancing and retreating sides, leading to microhardness differences of about 10 $HV_{0.2}$ is strongly influenced by tool geometries and welding parameters [4,8]. Nevertheless, the width of the HAZ is smaller in the AS as evident from the microhardness profile. In the SZ, dynamic recrystallization resulting in fine grains appears to be responsible for higher microhardness in relation to the TMAZ [12]. However, the post-weld natural aging that leads to GP zones and δ′ formation have also been reported as possible reasons for increased microhardness in the SZ [4,5,13,14].

Classification of FSW affected zones was based on tool and pin dimensions, 10 and 5 mm respectively, microhardness results and optical observations are presented in Figs. 3, 4 and 5. Based on this information, the temperatures reached in each zone were estimated.

3.3. Phase Characterization

TEM and electron diffraction (SAED) analyses performed in the regions of the welded alloy shown in Fig. 3 were correlated with the microhardness measurements across the surface of the weld. Results showed that the dominant phases in the BM are the T1 (Al_2CuLi), θ′ (Al_2Cu), δ′/β′ ($Al_3(Li,Zr)$) and Ω (Al_2Cu) phases as illustrated in Fig. 6. Corresponding [110] zone axis diffraction pattern is shown in Fig. 6b. Four variants of the T1 phase were observed: two variants produced superlattice spots at 1/3 and 2/3 of ⟨220⟩ and the other two variants appear as continuous streaks along ⟨111⟩. Also, streaks along ⟨001⟩ indicate the presence of GP zone or θ′ precipitation. Fig. 6d shows corresponding [112] zone axis diffraction pattern. Some superlattice spots and continuous streaks related to T1 phase in ⟨111⟩ direction can be observed. However, no streaks along ⟨042⟩ direction related to S′ (Al_2CuMg) phase was observed. The θ′ phase was observed in both [110] and [100] oriented zone axis diffraction patterns, Fig. 6b and f. Streaks along ⟨001⟩ indicate the presence of GP zone or θ' precipitation. Fig. 6f also shows that the four variants of T1 phase produced a set of four superlattice spots.

The δ′ and β′ phases were also observed in the BM. These are often identified as δ′/β′ due to similarities in morphology and electron diffraction [4,12]. Literature reports [9,18] that the δ′ phase precipitates on top of β′ phase during heat treatment, forming a core-shell morphology, and this was in fact observed, Fig. 7.

The β′ phase is formed during homogenization of cast alloys. They are stable as a result of low Zr solubility in Al, small misfit and sluggish diffusion of Zr in Al. Thus, during welding process this phase does not undergo dissolution. The δ′ phase is a metastable phase coherent with the matrix [18].

The Ω phase has a similar structure to that of T1. It forms as a hexagonal or orthorhombic plate on the {111} planes [13,27]. Its formation is associated to Mg and Ag additions in Al-alloys [18,27,48]. The θ′ is a metastable phase which might be either parallel or perpendicular to T1. In Al-Cu-Li alloys, additions of Mg promote the formation of θ′ phase; however when Ag is present, this effect is weakened

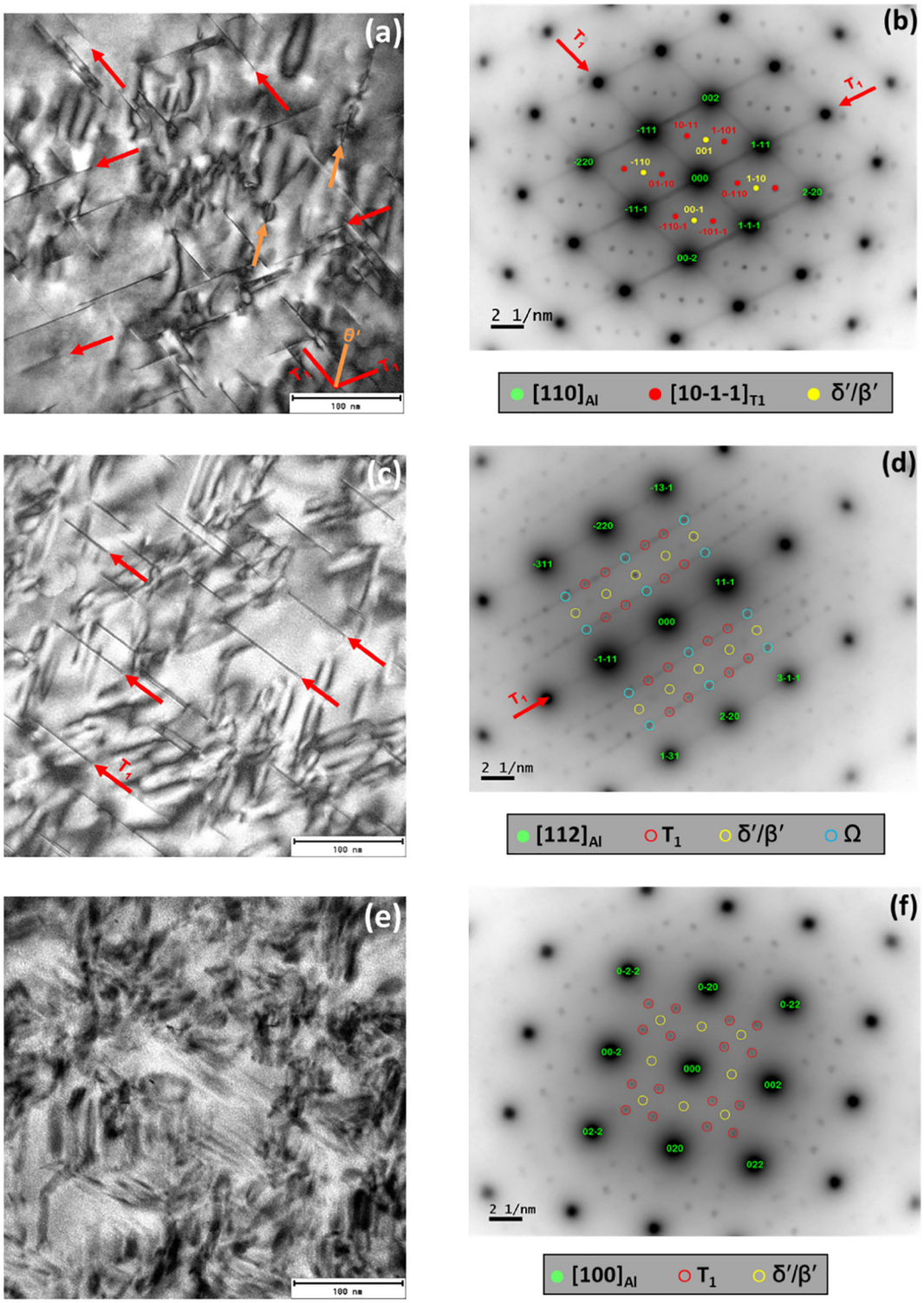

Fig. 9. TEM bright field images (a, c, e) and SAED (b, d, f) patterns obtained in different orientations from the RS and AS of the HAZ of AA2098-T351 alloy. In [110] zone axis bright field image of the RS (a), the presence of θ′ variant can be observed but not as a dominant phase, no streaks along ⟨001⟩ direction can be seen in the corresponding SAED pattern (b). The micrographs (c, d, e, f) taken from advancing side show no presence of θ′ variant.

due to the preferential attraction between Mg and Ag over that of Mg with Cu. This leads to less Mg atoms available to form Cu-Mg vacancy groups which assist the precipitation of θ′ [38].

The difficulty in identifying GP zones by TEM is reported in literature [25]. In order to further investigate the presence of these zones in the BM, DSC analysis was carried out and the results are presented in

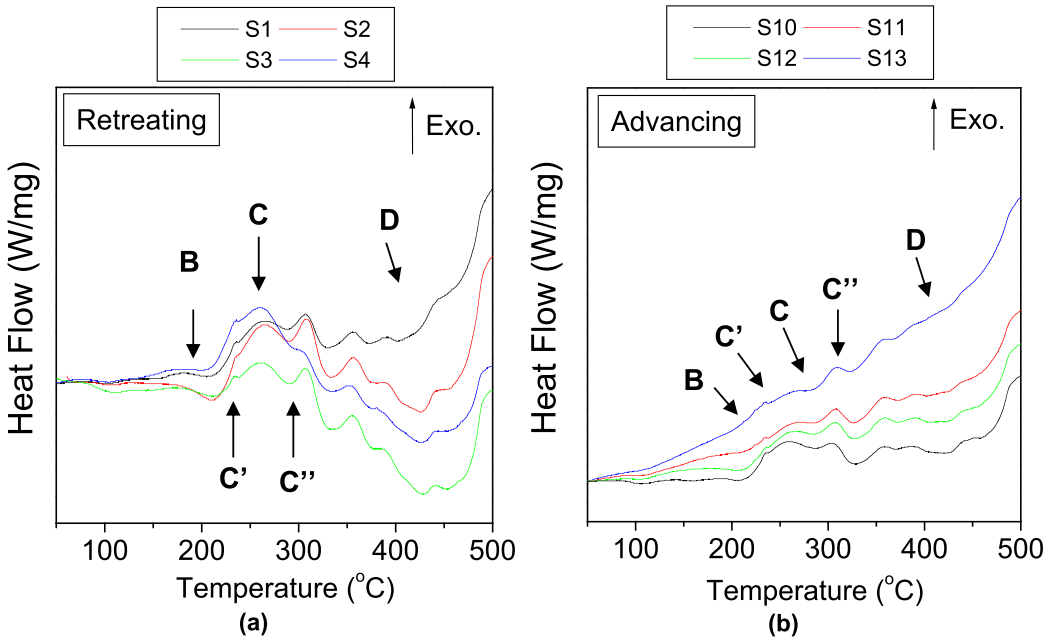

Fig. 10. DSC thermograms obtained at 10 °C/min for samples from the (a) RS and (b) AS regions of the HAZ. The samples were obtained from the regions labelled S1–4 and S10–13 as depicted in Fig. 4. The dimensions of each sample were 3 mm × 3 mm × 1 mm.

Fig. 8. No significant GP zones were observed in the BM. Increase in dislocation density is favored by stretching and this might explain the suppressed formation of large-sized clusters/GP zones [49–51]. According to Cersara and Fiorini [52], pre-straining could reduce the driving force behind natural aging and inhibit the formation of clusters/GP zones. According to literature [28,48], the presence of Ag and Mg favor T1 precipitation and, consequently, hinders GP zone formation.

In Fig. 8, the peak B between 200 °C and 250 °C confirms the presence of δ′ phase. This phase has been reported to precipitate at low temperatures [5,20,25,53]. Peak C, as well as its convolutions, C′ and C″, represents T1 phase precipitation that occurs in the 250 °C–350 °C range [5,20,28,54]. The slight peak precipitation is related to the "51" temper condition and alloying elements. This temper is associated with pre-straining between 1% and 3% of the permanent strain, prior to aging. This phase precipitates preferentially at grain/subgrain boundaries and dislocations [55–59]. Thus, the stretching step leads to increased dislocations density and, consequently, an increase in T1 phase precipitation [60]. Generally, dislocations reduce the strain energy associated with the interface between the matrix and T1 phase, and this promotes the nucleation and growth of the T1 phase [28]. The addition of Ag in presence of Mg favors precipitation of T1 phase, as previously reported. Finally, peak D is related to dissolution of T1, θ′ and Ω phases at high temperatures [5,26,37].

TEM results from the AS and RS sides of the HAZ showed that the main phases in these zones are T1, δ′/β′ and Ω, as Fig. 9 shows.

As it was observed in the BM, four variants of the T1 phase were also observed in the HAZ. According to Fig. 9b, two variants produced superlattice spots at 1/3 and 2/3 of ⟨220⟩ and the other two variants appear as continuous streaks along ⟨111⟩ exactly like what was observed for the BM. Again, exactly like the case of the BM, very faint streaks along ⟨001⟩ indicating the presence of GP zone or θ′ precipitation were also observed. The corresponding [112] zone axis diffraction pattern, Fig. 9d, shows the dominant phases as previously mentioned. The θ′ phase was observed in [110] orientation, however it is not a dominant phase. This phase was found randomly distributed only at certain regions. For the [001] zone axis diffraction pattern, four variants of T1 phase produced a set of four superlattice spots, Fig. 9f. The TEM results showed the same dominant phases in the RS and AS of the HAZ, Fig. 9. However, further information (provided by the DSC thermographs corresponding to these zones) showed significant differences between the RS and AS of HAZ, in accordance with differences indicated in the microhardness profile, Fig. 5.

Higher temperatures are reached in the AS compared to the RS. However, the domains of the effects of thermal cycles are wider in the RS compared with the AS. Fig. 10a shows increase in the peaks C′, C″ and C related to overaging, coarsening and partial dissolution of T1 phases. This effect extends to 12 mm from the edges of the weld and it is in accordance with the microhardness results. Temperatures in the range of 100 °C–300 °C are reached in these regions, according to thermal simulations, Fig. 5. In the AS, the effects of overaging are limited to the approximately 9 mm from the edge of the weld. In fact, the slope of microhardness variation with distance from the weld boundary was steeper in this side of the sample, Fig. 5. From DSC results, increase in peak dissolution corresponding to δ′ phase was observed for both sides. This is because, prior to welding, the BM contains δ′ phase which was formed at low temperatures. Subsequently, the welding process causes the coarsening of the pre-existing δ′ phase, whose volume fraction was further enhanced by a combination of the partial dissolution of the T1 phase during the welding and the natural aging process after welding [13–15]. The partial dissolution of the T1 particles increases the amount of Li atoms in the solid solution, and this, in turn, favors the precipitation of δ′ phases at lower temperatures after the welding.

TEM images were obtained from the TMAZ of the RS (Fig. 11) and

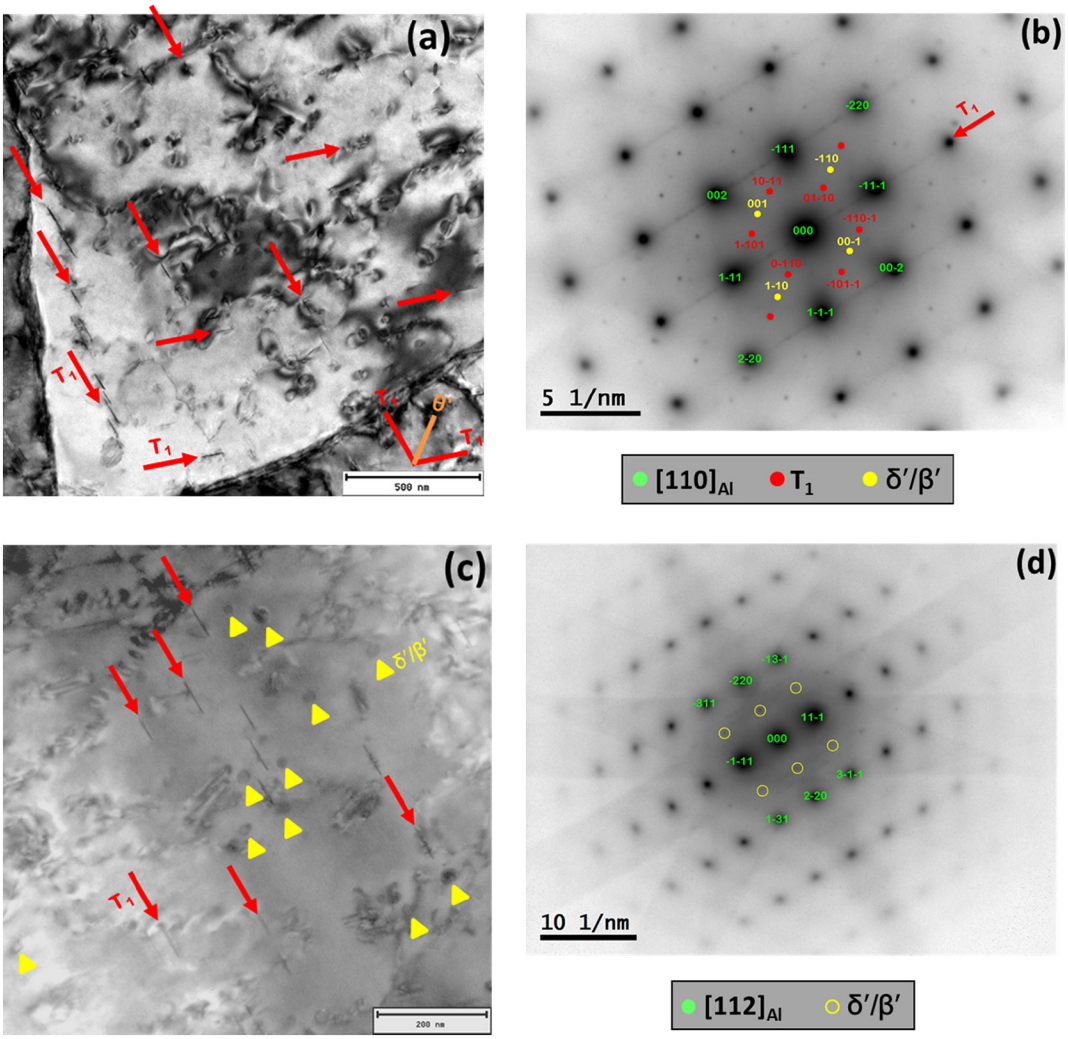

Fig. 11. TEM bright field images (a, c) and corresponding SAED patterns (b, d) obtained from the TMAZ of the RS in AA2098-T351 alloy. The presence of T1 phase can be observed in the images a, c obtained in different orientations, but being a weaker phase its characteristic streaking feature along ⟨111⟩ is clearly visible only in one direction of the [110] zone axis SAED pattern (b).

that of the AS (Fig. 12). Slight differences were observed in both figures. The dominant phases in the RS were the δ′/β′ and T1 phases. Nevertheless, in the AS only the δ′/β′ phase prevailed. However, it is important to mention that the features in the TMAZ regions, irrespective of the side (AS or RS), can vary depending on the temperature reached and the extent of deformation experienced by the exact region in which the TEM images were obtained. In the RS images corresponding to [110] zone axis diffraction pattern, Fig. 11b, three T1 variants (two superlattice spots along ⟨220⟩ and one streak along ⟨111⟩ directions) were observed. Also, GP zone or θ′ in ⟨001⟩ was not observed. For [112] zone axis, the presence of T1 phase can be seen in the bright-field image (Fig. 11c), but its related streaks along ⟨111⟩ direction were difficult to find in the corresponding diffraction pattern (Fig. 11d) due to weak intensities. Although the T1 phase was found in the RS of the TMAZ, it was not a predominating phase; and in the advancing side of the TMAZ, there was no evidence of the T1 phase. This can be seen from the [110] zone axis bright-field image/diffraction pattern in Fig. 12a and b where the lack of streaks along ⟨111⟩ or superlattice spots in ⟨220⟩ indicated the absence of T1 phase. Also, no streaks were identified along ⟨001⟩ suggesting the absence of GP zone or θ′ precipitation. Thus, T1 and θ′ were absent in this zone. Extra spots arise due to the presence of δ′/β′ precipitates. Both δ′/β′ precipitates appear as spheres in the form of core-shell structure with β′ as core and δ′ as shell. For [112] zone axis diffraction pattern, no streaks were observed in any orientation. Hence, T1 and θ′ were absent. However, extra spots show the presence of δ′/β′ precipitates.

To support the affirmation that T1 phase is not a dominant phase in the AS, low magnification images of this zone are shown in Figs. 13 and 14.

For the SZ, the dominant phases were the T1, δ′/β′ and Ω. From [112] zone axis diffraction patterns acquired in different regions (Fig. 15a, c), the presence of isolated δ′/β′ precipitates (12b) and intermixing of δ′/β′ & Ω (Fig. 12d) phase precipitates were found. However, in both regions, T1 and θ' precipitates were not be identified. In [110] zone axis orientation of a different region, superlattice spots related to T1 phase were found (Fig. 15f). But due to large dynamical contrast of [110], clear identification of T1 precipitates in the bright-field image was not possible. By tilting along ⟨111⟩ direction and

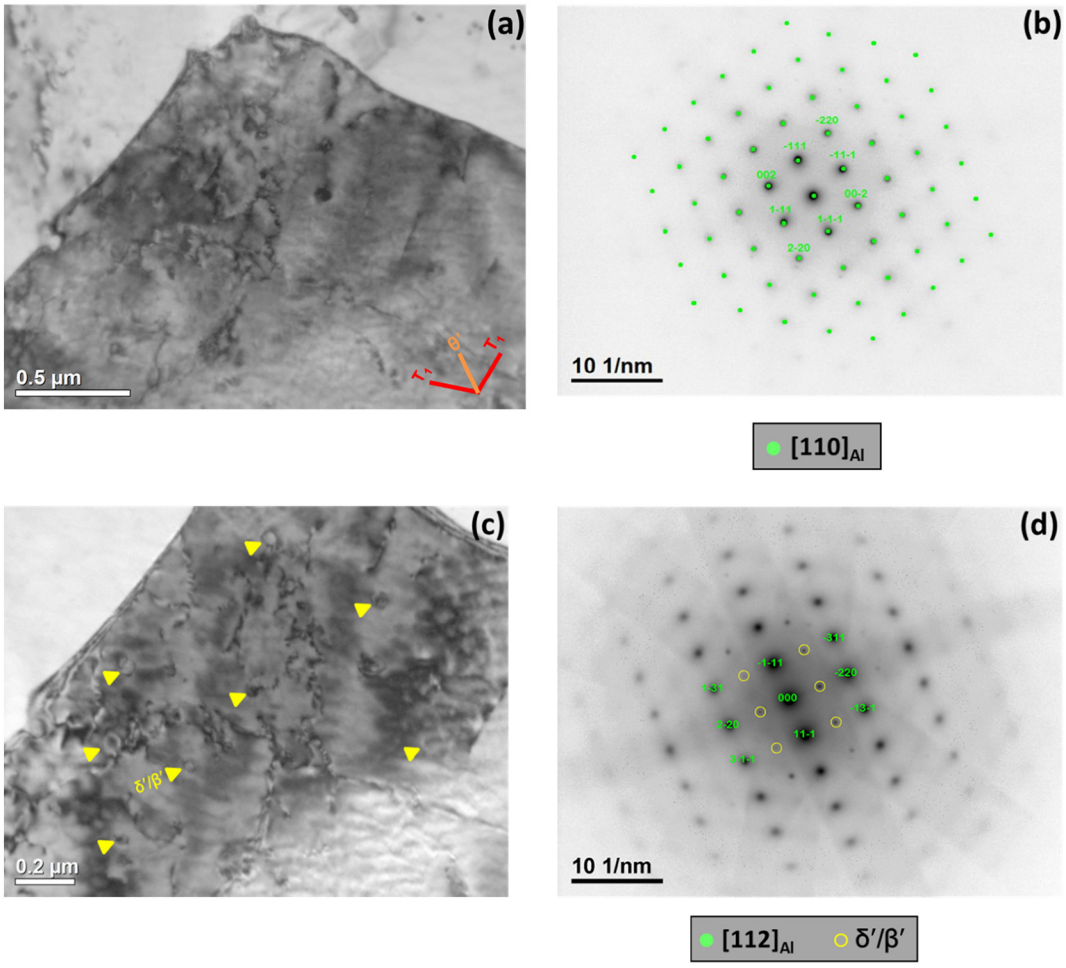

Fig. 12. [110], [112] TEM bright field images (a, c) and corresponding SAED patterns (b, c) obtained from TMAZ of the AS in the AA2098-T351 alloy. Like in the bright field images of the TMAZ in the RS (Fig. 11a, c), no T_1 phase variants are visible.

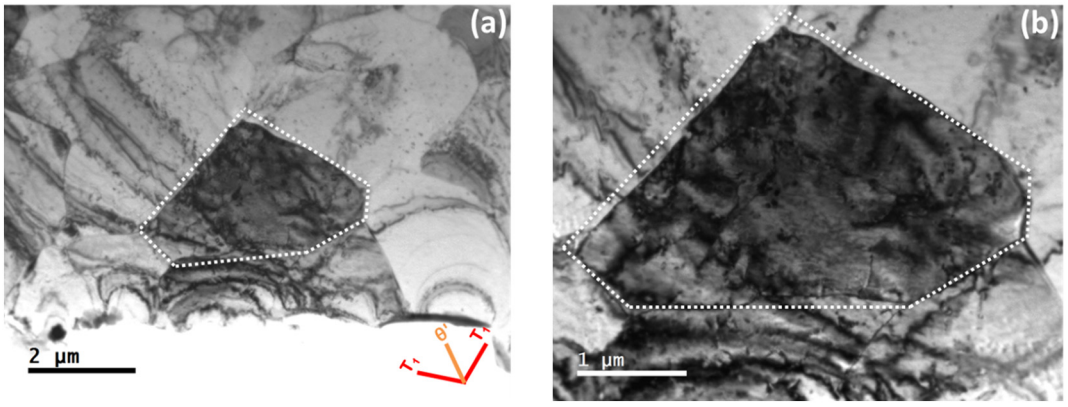

Fig. 13. Low magnification TEM images of TMAZ of the AS related to Fig. 12. The grain oriented along [110] zone axis appear darker in contrast and is highlighted by a dotted line. Adjacent grains which are not oriented along the zone axis appear brighter and the edge-on features associated with T_1 or θ′ variants are easy to understand. However, no such features are visible in either darker or brighter contrast grains.

establishing kinematical diffraction condition, it was possible to identify the T1 phase precipitates (Fig. 15e).

TEM analysis indicated absence of GP zones in the SZ. However, DSC thermograms from SZ show a pronounced dissolution peak between 100 °C–150 °C (peak A), Fig. 16, related to GP zones [15,21,23,28]. As previously mentioned, GP zones are hardly identified by TEM [25]. These zones are formed during cooling from supersaturated slid solution (SSS) due to the high temperatures reached at

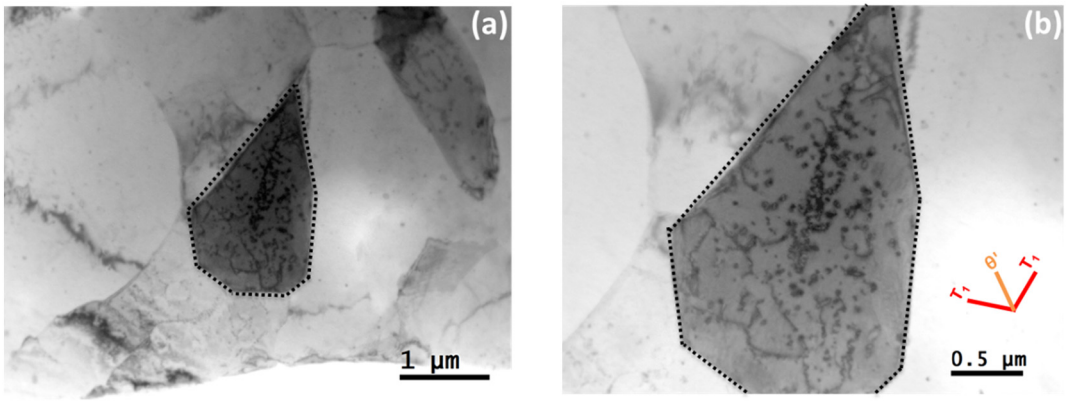

Fig. 14. Others low magnification TEM images of TMAZ of the AS. The grain oriented along [110] zone axis appear darker in contrast and is highlighted by a dotted line. Apart from some defects (inside the oriented grain) and δ′/β′ phase characteristics, no streaking features associated with T_1 or θ′ variants are visible.

weld joint that leads to T1 and δ′ phase dissolution [4]. The GP zones are formed due to natural aging. In fact, the temperatures reached in the weld joint, Table 1, contribute to natural aging in this zone by somewhat enhancing the formation of SSS. The precipitation in Al-Cu-Li alloys is dependent on Cu/Li ratio [23]. For alloys with Cu/Li ratio between 2.5 and 4, the precipitation sequence proposed is:

$$SSS \rightarrow GP\ zones \rightarrow GP\ zones + \delta' \rightarrow \theta'' + \delta' \rightarrow \theta' + \delta' \rightarrow \delta' + T1 \rightarrow T1 \quad (4)$$

Depending on heat-treatment conditions, the solution treated material can decompose and precipitate via several different reactions [27]. The large precipitation peak (peak C) related to T1 phase shows that the temperatures reached, Table 1, contribute to T1 phase dissolution. Thus, supersaturated solid solution is formed and the precipitation sequence as shown above can occur. The prominent peak C, also leads to the conclusion that T1 phase density decreases in the SZ in relation to the BM, and this was supported by TEM analyses. The steeper microhardness variation with distance in the AS compared to the RS is supported by the small A and B peaks of the TMAZ in the AS (S8 and S9). The precipitation of GP zones and δ′ phase were less favored in the AS compared with the RS of the weld joint. This is evident when curves S8–9 (AS) are compared with curves S5–7(RS) in the thermograph in Fig. 16.

Table 2 indicates the main phases found in the various zones of the AA2098-T351 alloy welded by FSW and their characteristics based on results from DSC and TEM analyses.

4. Conclusions

The microstructural characterization of the zones of AA2098-T351 welded by FSW was carried out by TEM and DSC analyses and the results were correlated to microhardness measurements. Thermal modelling was also carried out and the results were compared with thermal measurement results obtained during the welding process. The results showed that in the base metal (BM), the prevailing phases are T1 (Al_2CuLi) θ′ (Al_2Cu), δ′/β′ (Al_3(Li,Zr)) and Ω (Al_2Cu). Similar phases, with the exception of the θ′ phase, were identified in the heat affected zones (HAZ) of the retreating side (RS) and advancing side (AS). However, the density of the T1 particles were reduced in the HAZ compared with the BM. Given that the T1 phase is the major strengthening phase, this led to decrease in microhardness values in the HAZ compared with the BM. This revelation was strongly supported by DSC thermograms which showed that the T1 phase present in the BM was partially dissolved in the HAZ due the welding process. Slight differences in precipitation sequence were observed in the TMAZ regions of the AS and RS supporting the asymmetric behavior which was observed in the microhardness profile. This is related to the varying degrees of the effect of thermal cycles experienced at the two sides (AS and RS) of the weld. Thermal modelling and thermal measurements results, which were in complete agreement, confirmed this asymmetry. The dominant phases in the TMAZ of the RS were δ′/ β′ and T1. On the contrary, T1 phase was rarely found in the TMAZ of the AS. This led to lower microhardness values as the predominant strengthening phase present was the δ′/β′ phase (known as one of main hardening phase in absence of T1). In the SZ, GP zones, T1, δ′/β′ (Al_3(Li,Zr)) and Ω were observed. In comparison with the TMAZ, the presence of these phases in the SZ led to higher microhardness. Higher DSC peaks related to T1 phase precipitation were observed in the SZ which confirms that most of the T1 particles present in the BM phase were dissolved. Moreover, higher GP zones and δ′ DSC dissolution peaks were also observed in the SZ compared with the other analyzed zones, and this showed that the temperature reached at this zone favors the precipitation of these phases. This is because the temperature reached during the welding process leads to the dissolution of the T1 phase which in turn favors the precipitation of these phases (GP zones and δ′ phase) after welding. Finally, DSC showed to be an effective technique for characterization of GP zones and acted as a complementary method in microstructural characterization of the aluminum alloy used in this study.

Data Availability

The raw/processed data required to reproduce these findings cannot be shared at this time as the data also forms part of an ongoing study.

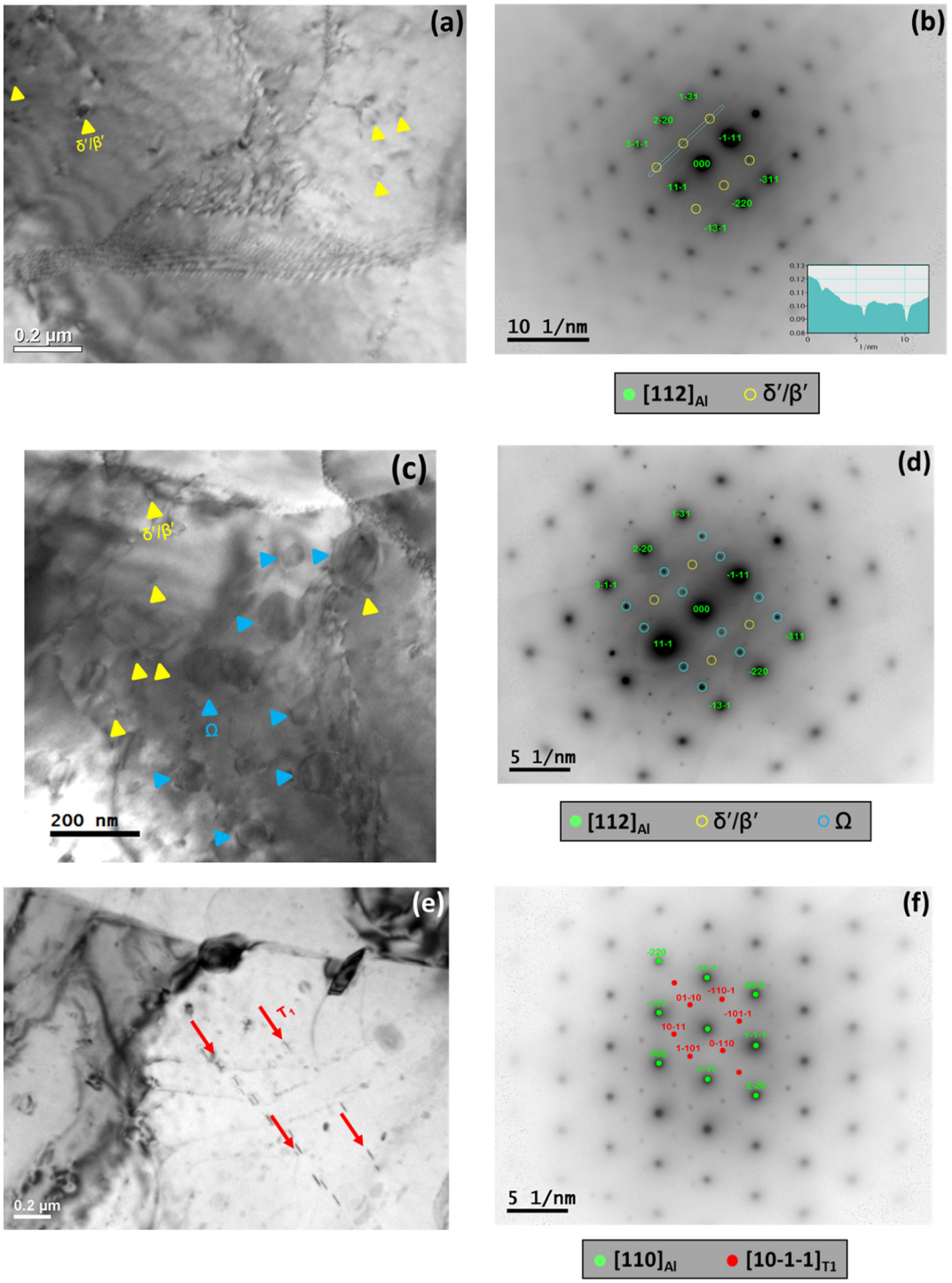

Fig. 15. TEM bright field images (a, c, e) and SAED patterns (b, d, f) showing the dominant phases in the SZ of the AA2098-T351 alloy. Weak intensities related to δ′/β′ precipitates are highlighted by plotting an intensity profile across the superlattice spots (b). The presence of Ω phase is evident when the electron beam is approximately parallel to $[112]_{\alpha}$ orientation (c). From the bright field image (e) taken in kinematical imaging conditions i.e. away from exactly [112] zone axis orientation along ⟨111⟩, one T1 variant is observed.

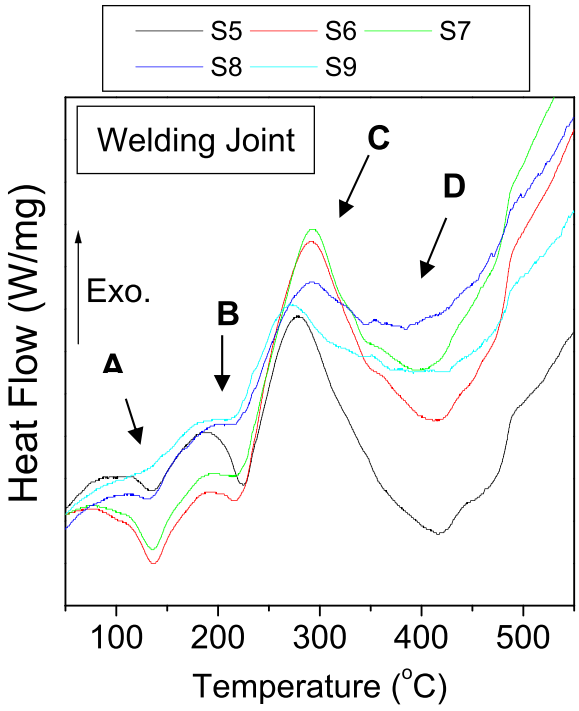

Fig. 16. DSC thermograms obtained at 10 °C/min for samples from the welding joint of AA2098-T351 alloy. The dimensions of each samples were 3.0 mm × 3.0 mm × 1.0 mm.

Table 2
Main phases characteristics found in the various zones of the AA2098-T351 alloy welded by FSW.

Precipitate	Composition	Form	Lattice parameters	Location
δ′	Al_3Li	Spheres in the form of shell	–	SZ, TMAZ HAZ, BM
β′	Al_3Zr	Spheres in the form of core	–	SZ, TMAZ HAZ, BM
Ω	Al_2Cu	Orthorhombic	a = 0.496 nm b = 0.859 nm c = 0.848 nm α = β = γ = 90	SZ, HAZ BM
T1	Al_2CuLi	Hexagonal phase	a = b = 0.4954 nm c = 0.9327 nm α = β = 90° γ = 120°	SZ, HAZ TMAZ(Ret) BM
GP zones	Cu	Single layer on [100]Al	–	TMAZ, SZ
θ′	Al_2Cu	Tetragonal	a = 0.404 nm c = 0.58 nm α = β = γ = 90	BM

Acknowledgments

The authors acknowledge CAPES (Capes/Cofecub N° 806-14) and FAPESP (2013/13235-6) for financial support for this work and to CAPES for the grants of M.X. Milagre (99999.000332/2016-00), C.S.C. Machado (99999.000400/2016-05) and FAPESP for the grants of U. Donatus (Proc.2017/03095-3). Acknowledgements are also due to Dr. Duclerc Fernandes Parra, Eleosmar Gaspari and Olandir V. Correa from IPEN for technical support in DSC analysis. Also to Dr. Nadine Pebere, Dr. Emilie Lebon from the Institut National Polytechnique de Toulouse (INPT) and Sophie Regnier from the Institut Catholique d'Arts et Métiers (ICAM) for technical support in microhardness analysis. Moreover, Dr. Antonello Astarita from University of Naples "Federico II", Italy Dept. of Chemical, Materials and Industrial Production Engineering for providing the test material.

References

[1] R. Nandan, T. Debroy, H.K.D.H. Bhadeshia, Recent advances in friction stir welding – process, weldment structure and properties, Prog. Mater. Sci. 53 (2008) 980–1023, http://dx.doi.org/10.1016/j.pmatsci.2008.05.001.
[2] R.S. Mishra, Z.Y. Ma, Friction stir welding and processing, Mater. Sci. Eng. R. Rep. 50 (2005) 1–78, http://dx.doi.org/10.1016/j.mser.2005.07.001.
[3] P.L. Threadgill, A.J. Leonard, H.R. Shercliff, P.J. Withers, Friction stir welding of aluminium alloys, Int. Mater. Rev. 54 (2009) 49–93, http://dx.doi.org/10.1179/174328009X411136.
[4] R.W. Fonda, J.F. Bingert, Precipitation and grain refinement in a 2195 Al friction stir weld, Metall. Mater. Trans. A Phys. Metall. Mater. Sci. 37 (2006) 3593–3604, http://dx.doi.org/10.1007/s11661-006-1054-2.
[5] A. Steuwer, M. Dumont, J. Altenkirch, S. Birosca, A. Deschamps, P.B. Prangnell, P.J. Withers, A combined approach to microstructure mapping of an Al-Li AA2199 friction stir weld, Acta Mater. 59 (2011) 3002–3011, http://dx.doi.org/10.1016/j.actamat.2011.01.040.
[6] M. Jariyaboon, A.J. Davenport, R. Ambat, B.J. Connolly, S.W. Williams, D.A. Price, The effect of welding parameters on the corrosion behaviour of friction stir welded AA2024-T351, Corros. Sci. 49 (2007) 877–909, http://dx.doi.org/10.1016/j.corsci.2006.05.038.
[7] P. Cavaliere, M. Cabibbo, F. Panella, A. Squillace, 2198 Al-Li plates joined by friction stir welding: mechanical and microstructural behavior, Mater. Des. 30 (2009) 3622–3631, http://dx.doi.org/10.1016/j.matdes.2009.02.021.
[8] W. Li, R. Jiang, Z. Zhang, Y. Ma, Effect of rotation speed to welding speed ratio on microstructure and mechanical behavior of friction stir welded aluminum-lithium alloy joints, Adv. Eng. Mater. 15 (2013) 1051–1058, http://dx.doi.org/10.1002/adem.201300147.
[9] J.C. Rao, E.J. Payton, C. Somsen, K. Neuking, G. Eggeler, A. Kostka, J.F. Dos Santos, Where does the Lithium go? - a study of the precipitates in the stir zone of a friction stir weld in a li-containing 2xxx series Al alloy, Adv. Eng. Mater. 12 (2010) 298–303, http://dx.doi.org/10.1002/adem.200900284.
[10] Y. Ma, X. Zhou, Y. Liao, Y. Yi, H. Wu, Z. Wang, W. Huang, Localised corrosion in AA 2099-T83 aluminium-lithium alloy: the role of grain orientation, Corros. Sci. 107 (2015) 41–48, http://dx.doi.org/10.1016/j.corsci.2016.02.018.
[11] R.J. Rioja, J. Liu, The evolution of Al-Li base products for aerospace and space applications, Metall. Mater. Trans. A Phys. Metall. Mater. Sci. 43 (2012) 3325–3337, http://dx.doi.org/10.1007/s11661-012-1155-z.
[12] C. Gao, Z. Zhu, J. Han, H. Li, Correlation of microstructure and mechanical properties in friction stir welded 2198-T8 Al-Li alloy, Mater. Sci. Eng. A 639 (2015) 489–499, http://dx.doi.org/10.1016/j.msea.2015.05.038.
[13] A.K. Shukla, W.A. Baeslack, Study of process/structure/property relationships in friction stir welded thin sheet Al-Cu-Li alloy, Sci. Technol. Weld. Join. 14 (2009) 376–387, http://dx.doi.org/10.1179/136217109X412409.
[14] A.K. Shukla, W.A. Baeslack, Study of microstructural evolution in friction-stir welded thin-sheet Al-Cu-Li alloy using transmission-electron microscopy, Scr. Mater. 56 (2007) 513–516, http://dx.doi.org/10.1016/j.scriptamat.2006.11.028.
[15] B. Noble, S.J. Harris, S. Katsikis, K. Dinsdale, Low temperature thermal stability of quaternary Al-Li-Cu-Mg-alloys, Mater. Sci. Forum 519–521 (2006) 209–214, http://dx.doi.org/10.4028/www.scientific.net/MSF.519-521.209.
[16] B. Noble, S.E. Bray, On the α(Al)/δ′(Al3Li) metastable solvus in aluminium-lithium alloys, Acta Mater. 46 (1998) 6163–6171, http://dx.doi.org/10.1016/S1359-6454(98)00263-8.
[17] M.J. Starink, Analysis of aluminium based alloys by calorimetry: quantitative analysis of reactions and reaction kinetics, Int. Mater. Rev. 49 (2004) 191–226, http://dx.doi.org/10.1179/095066004225010532.
[18] S.C. Wang, M.J. Starink, Precipitates and intermetallic phases in precipitation hardening Al–Cu–Mg–(Li) based alloys, Int. Mater. Rev. 50 (2005) 193–215, http://dx.doi.org/10.1179/174328005X14357.
[19] E.A. Starke, J.T. Staleyt, Application of modern aluminum alloys to aircraft, Prog. Aerosp. Sci. 32 (1996) 131–172.
[20] H. Qin, H. Zhang, H. Wu, The evolution of precipitation and microstructure in friction stir welded 2195-T8 Al-Li alloy, Mater. Sci. Eng. A 626 (2015) 322–329, http://dx.doi.org/10.1016/j.msea.2014.12.026.
[21] G. Riontino, S. Abis, P. Mengucci, DSC investigation of natural ageing in high-copper AlCuMg alloys, Mater. Sci. Forum 331–337 (II) (2000) 1025–1030, http://dx.doi.org/10.4028/www.scientific.net/MSF.331-337.1025.
[22] Y.P. Wu, L.Y. Ye, Y.Z. Jia, L. Liu, X.M. Zhang, Precipitation kinetics of 2519A aluminum alloy based on aging curves and DSC analysis, Trans. Nonferrous Metals Soc. China 24 (2014) 3076–3083 English Ed. https://doi.org/10.1016/S1003-6326(14)63445-2.
[23] H.H. Jo, K.-I. Hirano, Precipitation processes in Al-Cu-Li Alloy Studied by DSC, Mater. Sci. Forum 13–14 (1987) 377–382, http://dx.doi.org/10.4028/www.scientific.net/MSF.13-14.377.
[24] K.S. GHOSH, K. DAS, U.K. CHATTERJEE, Characterization of retrogression and reaging behavior of 8090 Al-Li-Cu-Mg-Zr, Metall. Mater. Trans. A. 35 (2004) 3681–3691.
[25] M.J. Starink, P. Wang, I. Sinclair, P.J. Gregson, Microstructure and strengthening of Al-Li-Cu-Mg alloys and MMCS: I. Analysis and modelling of microstructural changes, Acta Mater. 47 (1999) 3841–3853, http://dx.doi.org/10.1016/S1359-6454(99)00227-X.

[26] W. tao Wang, X. ming Zhang, Z. guo Gao, Y. zhen Jia, L. ying Ye, D. wei Zheng, L. Liu, Influences of Ce addition on the microstructures and mechanical properties of 2519A aluminum alloy plate, J. Alloys Compd. 491 (2010) 366–371, http://dx.doi.org/10.1016/j.jallcom.2009.10.185.
[27] P.S. CHEN, B.N. Bhat, Time-temperature-precipitation behavior in AI-Li alloy 2195, Tech. Rep., TM 2002-211546, (2002) http://ntrs.nasa.gov/archive/nasa/casi.ntrs.nasa.gov/20020030744.pdf.
[28] H. Sidhar, R.S. Mishra, Aging kinetics of friction stir welded Al-Cu-Li-Mg-Ag and Al-Cu-Li-Mg alloys, Mater. Des. 110 (2016) 60–71, http://dx.doi.org/10.1016/j.matdes.2016.07.126.
[29] Y. Tao, D.R. Ni, B.L. Xiao, Z.Y. Ma, W. Wu, R.X. Zhang, Y.S. Zeng, Origin of unusual fracture in stirred zone for friction stir welded 2198-T8 Al-Li alloy joints, Mater. Sci. Eng. A 693 (2017) 1–13, http://dx.doi.org/10.1016/j.msea.2017.03.079.
[30] Y.E. Ma, Z.C. Xia, R.R. Jiang, W.Y. Li, Effect of welding parameters on mechanical and fatigue properties of friction stir welded 2198 T8 aluminum–lithium alloy joints, Eng. Fract. Mech. 114 (2013) 1–11, http://dx.doi.org/10.1016/j.engfracmech.2013.10.010.
[31] Y.E. Ma, Z. Zhao, B. Liu, W. Li, Mechanical properties and fatigue crack growth rates in friction stir welded nugget of 2198-T8 Al-Li alloy joints, Mater. Sci. Eng. A 569 (2013) 41–47, http://dx.doi.org/10.1016/j.msea.2013.01.044.
[32] S. fei Zhang, W. dong Zeng, W. hua Yang, C. ling Shi, H. jun Wang, Ageing response of a Al-Cu-Li 2198 alloy, Mater. Des. 63 (2014) 368–374, http://dx.doi.org/10.1016/j.matdes.2014.04.063.
[33] N.D. Alexopoulos, A. Proiou, W. Dietzel, C. Blawert, V. Heitmann, M. Zheludkevich, S.K. Kourkoulis, Mechanical properties degradation of (Al-Cu-Li) 2198 alloy due to corrosion exposure, Procedia Struct. Integr. 2 (2016) 597–603, http://dx.doi.org/10.1016/j.prostr.2016.06.077.
[34] H.G. Salem, J.S. Lyons, Effect of equal channel angular extrusion on the microstructure and superplasticity of an Al-Li alloy, J. Mater. Eng. Perform. 11 (2002) 384–391, http://dx.doi.org/10.1361/105994902770343908.
[35] P.S.S. De, R.S.S. Mishra, J.A.A. Baumann, Characterization of high cycle fatigue behavior of a new generation aluminum lithium alloy, Acta Mater. 59 (2011) 5946–5960, http://dx.doi.org/10.1016/j.actamat.2011.06.003.
[36] R. Nandan, G.G. Roy, T.J. Lienert, T. Debroy, Three-dimensional heat and material flow during friction stir welding of mild steel, Acta Mater. 55 (2007) 883–895, http://dx.doi.org/10.1016/j.actamat.2006.09.009.
[37] P.a. Colegrove, H.R. Shercliff, 3-Dimensional CFD modelling of flow round a threaded friction stir welding tool profile, J. Mater. Process. Technol. 169 (2005) 320–327, http://dx.doi.org/10.1016/j.jmatprotec.2005.03.015.
[38] G. Chen, Q. Shi, Y. Li, Y. Sun, Q. Dai, J. Jia, Y. Zhu, J. Wu, Computational fluid dynamics studies on heat generation during friction stir welding of aluminum alloy, Comput. Mater. Sci. 79 (2013) 540–546, http://dx.doi.org/10.1016/j.commatsci.2013.07.004.
[39] M. Al-moussawi, A.J. Smith, A. Young, S. Cater, M. Faraji, Modelling of friction stir welding of DH36 steel, Int. J. Adv. Manuf. Technol. (2017) 1–20, http://dx.doi.org/10.1007/s00170-017-0147-y.
[40] H.B. Schmidt, J.H. Hattel, Thermal modelling of friction stir welding, Scr. Mater. 58 (2008) 332–337, http://dx.doi.org/10.1016/j.scriptamat.2007.10.008.
[41] C.M. Sellars, W.J.M. Tegart, Hot workability, Int. Metall. Rev. 17 (1972) 1–24, http://dx.doi.org/10.1179/imtlr.1972.17.1.1.
[42] J.S. Sheng-li YANG, Flow behavior and constitutive equations of Al Cu Li Mg Mn Zn alloy during isothermal compression, Chin. J. Nonferrous Met. (2015) 25.
[43] A.N. Albakri, B. Mansoor, H. Nassar, M.K. Khraisheh, Thermo-mechanical and Metallurgical Aspects in Friction Stir Processing of AZ31 Mg Alloy—A Numerical and Experimental Investigation, (2013), http://dx.doi.org/10.1016/j.jmatprotec.2012.09.015.
[44] D.R.G. Mitchell, DiffTools: electron diffraction software tools for DigitalMicrograph, Microsc. Res. Tech. 71 (2008) 588–593, http://dx.doi.org/10.1002/jemt.20591.
[45] A. Askari, S. Silling, B. London, M. Mahoney, Friction Stir Welding and Processing, TMS, Warrendale, PA, 2001.
[46] U. Donatus, G.E. Thompson, X. Zhou, J. Wang, K. Beamish, Flow patterns in friction stir welds of AA5083 and AA6082 alloys, Mater. Des. 83 (2015) 203–213, http://dx.doi.org/10.1016/j.matdes.2015.06.006.
[47] X.Y. Liu, M.J. Li, F. Gao, S.X. Liang, X.L. Zhang, H.X. Cui, Effects of aging treatment on the intergranular corrosion behavior of Al-Cu-Mg-Ag alloy, J. Alloys Compd. 639 (2015) 263–267, http://dx.doi.org/10.1016/j.jallcom.2015.03.174.
[48] B.P. Huang, Z.Q. Zheng, Independent and combined roles of trace Mg and Ag additions in properties precipitation process and precipitation kinetics of Al-Cu-Li-(Mg)-(Ag)-Zr-Ti alloys, Acta Mater. 46 (1998) 4381–4393, http://dx.doi.org/10.1016/S1359-6454(98)00079-2.
[49] D. Yin, Q. Xiao, Y. Chen, H. Liu, D. Yi, B. Wang, S. Pan, Effect of natural ageing and pre-straining on the hardening behaviour and microstructural response during artificial ageing of an Al-Mg-Si-Cu alloy, Mater. Des. 95 (2016) 329–339, http://dx.doi.org/10.1016/j.matdes.2016.01.119.
[50] Y. Birol, Pre-straining to improve the bake hardening response of a twin-roll cast Al-Mg-Si alloy, Scr. Mater. 52 (2005) 169–173, http://dx.doi.org/10.1016/j.scriptamat.2004.10.001.
[51] T. Masuda, Y. Takaki, T. Sakurai, S. Hirosawa, Combined effect of pre-straining and pre-aging on bake-hardening behavior of an Al-0.6 mass%Mg-1.0 mass%Si alloy, Mater. Trans. 51 (2010) 325–332, http://dx.doi.org/10.2320/matertrans.L-M2009831.
[52] S. Ceresara, P. Fiorini, Resistometric investigation of the ageing process after quenching and cold-work in AlZnMg alloys, Mater. Sci. Eng. 10 (1972) 205–210, http://dx.doi.org/10.1016/0025-5416(72)90090-0.
[53] M.J. Starink, A.J. Hobson, P.J. Gregson, DSC sample preparation for Al-based alloys, Scr. Mater. 34 (1996) 1711–1716, http://dx.doi.org/10.1016/1359-6462(96)00036-X.
[54] B. Malard, F. De Geuser, A. Deschamps, Microstructure distribution in an AA2050 T34 friction stir weld and its evolution during post-welding heat treatment, Acta Mater. 101 (2015) 90–100, http://dx.doi.org/10.1016/j.actamat.2015.08.068.
[55] J.M. Meininger, S.L. Dickerson, J.C. Gibeling, Observations of tension/compression asymmetry in the cyclic deformation of aluminum alloy 7075, Fatigue Fract. Eng. Mater. Struct. 19 (1996) 85–97, http://dx.doi.org/10.1111/j.1460-2695.1996.tb00934.x.
[56] B.M. Gable, A.W. Zhu, A.A. Csontros, E.A. Starke, The role of plastic deformation on the competitive microstructural evolution and mechanical properties, J. Light. Met. 1 (2001) 1.
[57] B.M. Gable, A.A. Csontros, E.A. Starke, A quench sensitivity study on the novel Al–Li–Cu–X alloy AF/C 458J, J. Light. Met. 2 (2002) 65.
[58] A.A. Csontros, E.A. Starke, The effect of inhomogeneous plastic deformation on the ductility and fracture behavior of age hardenable aluminum alloys, Int. J. Plast. 21 (2005) 1097–1118.
[59] M.A. Muñoz-Morris, I. Gutierrez-Urrutia, N. Calderon, D.G. Morris, Refinement of precipitates and deformation substructure in an Al–Cu–Li alloy during heavy rolling at elevated, Mater. Sci. Eng. A 492 (2008) 268–275.
[60] K.S. Al-Rubaie, M.A. Del Grande, D.N. Travessa, K.R. Cardoso, Effect of pre-strain on the fatigue life of 7050-T7451 aluminium alloy, Mater. Sci. Eng. A 464 (2004) 141–150.